European Journal of Mechanics / A Solids 82 (2020) 104005

Contents lists available at ScienceDirect

European Journal of Mechanics / A Solids

journal homepage: http://www.elsevier.com/locate/ejmsol

A dual interpolation boundary face method with Hermite-type approximation for elasticity problems

Jianming Zhang [a,*], Rui He [a], Weicheng Lin [a], Le Yang [a], Baotao Chi [a], Chuanming Ju [a], Suliman [b]

[a] State Key Laboratory of Advanced Design and Manufacturing for Vehicle Body, College of Mechanical and Vehicle Engineering, Hunan University, Changsha, 410082, China

[b] School of Mathematics and Statistics, Central South University, Changsha, 410083, China

ARTICLE INFO

Keywords:
Hermite-type approximation
Dual interpolation boundary face method
Boundary element method
Local stress concentration

ABSTRACT

This paper proposed the dual interpolation boundary face method with Hermite-type approximation for elasticity problems. Considering the physical relationship between displacement and traction, we also firstly present the Hermite-type approximation for elasticity problems. Compared with the standard moving least-squares (MLS) approximation, shape functions in Hermite-type approximation are directly constructed with Cartesian coordinates rather than parameter coordinates. This new approach can attain high accuracy and efficiency, the same as original dual interpolation boundary face method (DiBFM). Furthermore, the influence domain in the Hermite-type approximation can cover multiple edges. Thus, compared with the original DiBFM, this new scheme is more suitable for handling structures with thin walls and small features. Numerical examples with engineering background have illustrated the accuracy, efficiency and practicality of the method.

1. Introduction

The boundary element method (BEM) is widely applied to analyze practical engineering problems as a powerful numerical tool (Liu and Nishimura, 2006; Cheng et al., 2001; Wen et al., 1998; Zhang et al., 2011; Yao et al., 2004; Ribeiro et al., 2008). Compared with the finite element method (FEM), the BEM reduces the dimensions of the original problem by one. It can naturally solve fracture mechanics problems (Cruse, 2012; Cisilino and Aliabadi, 2004), contact problems (Garrido et al., 1991; Shu et al., 2016), and infinite domain problems (Dong et al., 2002; Telles and Brebbia, 1981). In the implementation of traditional BEM, the standard elements are used to approximate geometry of the boundary and perform the boundary integration, thus the geometric error is introduced. To overcome the defects, we have employed the boundary representation (B-rep) data structure which is widely used in standard solid modeling packages to eliminate geometry error (Zhang et al., 2009; Zhou et al., 2012; Wang et al., 2013; Li et al., 2015). Then, by coupling this technique with the boundary integral equation (BIE), we developed the boundary face method (BFM) in which the boundary of the domain is exactly represented in parametric form. In the BFM, the integrand quantities are calculated directly from the curves rather than from elements, thus it possesses higher integral accuracy than classical BEM. Moreover, the BEM can use both conforming and nonconforming elements (Manolis and Banerjee, 1986; Parreira, 1988; Florez and Power, 2001) as there is no need to ensure the continuity of trial functions. The former can obtain higher accuracy with the same source points, while it is hard to settle corner problems (Deng et al., 2013; Mitra and Ingber, 1993).

Taking the advantages of conforming and nonconforming elements, we presented the dual interpolation element (Zhang et al., 2017a, 2017b, 2019a, 2019b, 2019c) which is constructed by adding virtual nodes at the vertices and edges of a conventional nonconforming element. This novel element unified the conforming and nonconforming elements. Compared with the nonconforming element, it increased the interpolation order by two. Combining the dual interpolation elements and the BFM, we also established the dual interpolation boundary face method (DiBFM). This technique has successfully applied to potential problems (Zhang et al., 2017b), elasticity problems (Zhang et al., 2019a), crack problems (Zhang et al., 2019b) and contact problems (Zhang et al., 2019c).

The interpolation nodes in dual interpolation elements can be classified into source and virtual nodes and the boundary integral equations are only collocated at source nodes. There are double-layer interpolations in the DiBFM. The first is element interpolation, in which

* Corresponding author. College of Mechanical and Vehicle Engineering, Hunan University, Changsha, 410082, China.
E-mail address: zhangjm@hnu.edu.cn (J. Zhang).

https://doi.org/10.1016/j.euromechsol.2020.104005
Received 31 October 2019; Received in revised form 19 March 2020; Accepted 25 March 2020
Available online 17 April 2020

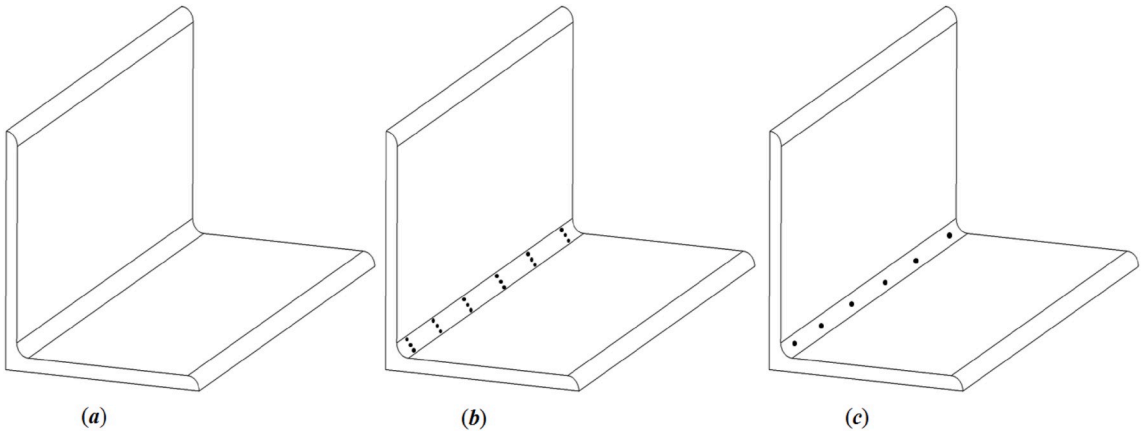

Fig. 1. Comparison of the least source points in different methods for angle steel with narrow faces: (a) geometric model, (b) three layers source points in the MLS approximation, (c) one layer source points in the Hermite-type approximation.

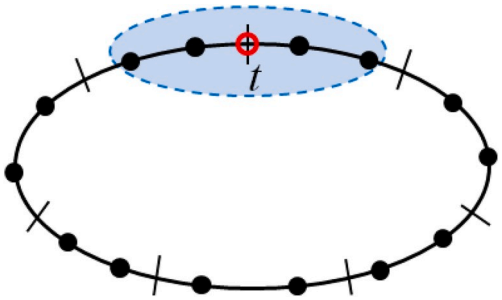

Fig. 2. The interpolation region for point t to approximate the physical variables.

the physical variables are interpolated by the source and virtual nodes. The second is meshless approximation, in which the physical variables of virtual nodes are approximated by those of source nodes. Thus, only the unknowns for source points appear in the final system of linear equations, and the DiBFM costs the same amount of computations as conventional BEM when solving the final equations.

The standard moving least-squares (MLS) approximation (Lancaster and Salkauskas, 1981; Belytschko et al., 1996; Duarte and Oden, 1996) is adopted as the second-layer interpolation in the original DiBFM. Although it possesses high accuracy and efficiency, there are still two weaknesses in it. On the one hand, the standard MLS approximation is performed in parameter space of geometry of the boundary, thus it is hard to deal with complex geometries whose parametric equations are hardly obtained. On the other hand, the influence domain in the MLS approximation is restricted in only one edge (for 2D problem) or face (for 3D problem). Thus, there are at least three layers source points allocated on a face so that the MLS approximation shape functions can be constructed (see Fig. 1 (b)). If the dense source points locate on a narrow face or short edge, evaluation of the nearly singular integrals will become difficult and the final system of linear equations will be ill-conditioned (Johnston et al., 2013; Ye, 2008).

To eliminate the difficulty encountered with the standard MLS approximation, Li and Aluru (Li and Aluru, 2002, 2003; Shrivastava and Aluru, 2003) presented the Hermite-type interpolation by considering the normal derivative of the unknown in the weighted least-squares minimization approach. The shape functions of the Hermite-type interpolation are directly constructed with Cartesian coordinates without resorting to parameter coordinates. Moreover, the influence domain in the Hermite-type interpolation can cover multiple edges (for 2D problems) or faces (for 3D problems). Therefore, the high interpolation accuracy can be still achieved even one layer source points locate on a face (see Fig. 1 (c)). However, the shape functions of Hermite-type interpolation in (Li and Aluru, 2002) lack the delta function property. Li and Aluru established additional equations to enforce the boundary conditions. Thus, extra calculation burden will be introduced (Li and Zhu, 2009). Furthermore, the physical relationship must be considered in constructing shape functions of the Hermite-type interpolation. In (Li and Aluru, 2002, 2003; Shrivastava and Aluru, 2003), only the Hermite-type interpolation for potential problem is presented.

In this paper, following the works of Li and Aluru, we firstly present the Hermite-type approximation for elasticity problems. Different form their work, the shape functions of the Hermite-type approximation in our method do not need to satisfy the delta function property. As a matter of fact, the DiBFM can combine with any meshless approximation technique. Then, based on our previous works (Zhang et al., 2019a), we also propose a novel dual interpolation boundary face method with Hermite-type approximation for elasticity problems. The major difference between the original and novel DiBFM is that a new Hermite-type approximation instead of MLS approximation is employed as the second-layer interpolation. Not only can the proposed method attain high accuracy and efficiency, the same as the original DiBFM, but also it is more suitable for handling structures with thin walls and small features.

An outline of this paper is as follows. We present the Hermite-type approximation for elasticity problems in Section 2. In Section 3, we introduce the dual interpolation method with Hermite-type approximation for elasticity problems. We present the dual interpolation boundary face method with Hermite-type approximation for elasticity problems in Section 4. Numerical examples are given in Section 5. Section 6 contains some conclusions and future works.

2. Hermite-type approximation for elasticity problems

The Hermite-type interpolation for potential problem is presented in (Li and Aluru, 2002, 2003; Shrivastava and Aluru, 2003). In this section, the shape functions of Hermite-type approximation for elasticity problems are firstly constructed in detail.

For 2D problems, given a point t, as shown in Fig. 2, the unknown displacements u_i and tractions t_i in the vicinity of the point t are approximated by

$$u_i(x,y) = \mathrm{p}_{u_i}^{\mathrm{T}}(x,y)\mathrm{a}_t, \tag{1}$$

$$t_i(x,y,n) = \mathrm{p}_{t_i}^{\mathrm{T}}(x,y,n)\mathrm{a}_t, \tag{2}$$

where $i = 1$–2 for 2D elasticity problems, $\mathrm{p}_{u_i}^{\mathrm{T}}$ and $\mathrm{p}_{t_i}^{\mathrm{T}}$ are the base interpolating polynomial of displacement and traction in i-th direction, respectively. a_t is the vector of unknown coefficient for point t and n is

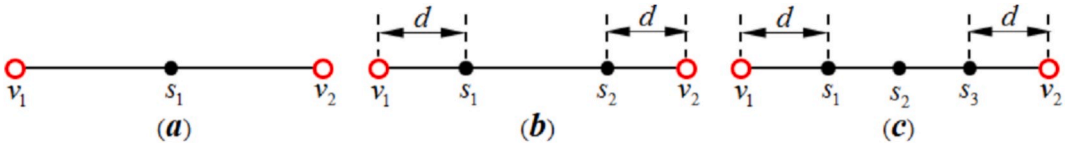

Fig. 3. Dual interpolation elements for 2D problems: (a) S1 element, (b) S2 element, and (c) S3 element.

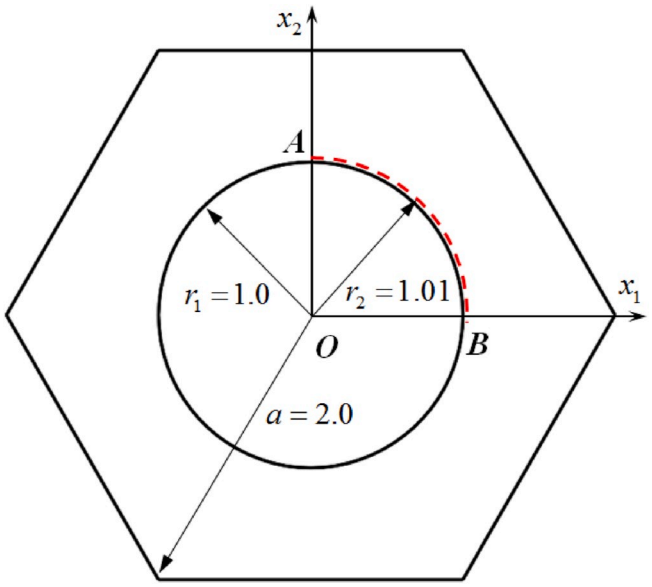

Fig. 4. A regular hexagon with circle on which the Dirichlet problem is solved.

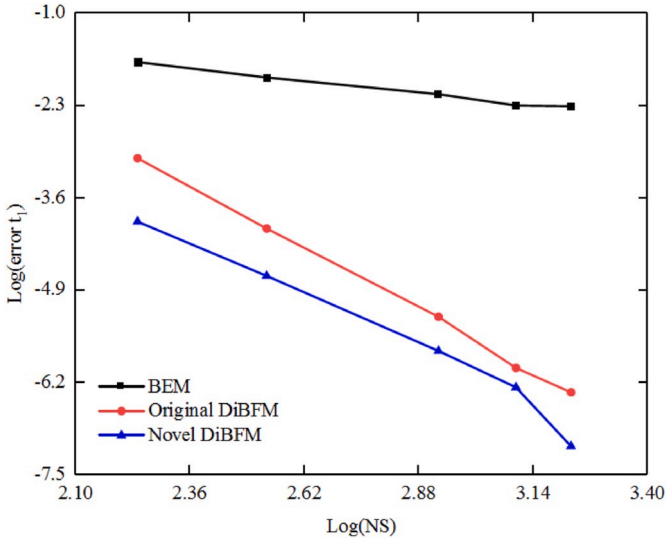

Fig. 5. Comparison of relative errors for traction t_1 obtained by different numerical methods.

the unit outward normal.

When a linear polynomial basis is adopted, $\mathrm{p}^{\mathrm{T}}_{u_1}$ and $\mathrm{p}^{\mathrm{T}}_{u_2}$ are given by

$$\mathrm{p}^{\mathrm{T}}_{u_1} = [1 \quad x \quad y \quad 0 \quad 0 \quad 0], m = 6, \tag{3}$$

$$\mathrm{p}^{\mathrm{T}}_{u_2} = [0 \quad 0 \quad 0 \quad 1 \quad x \quad y], m = 6. \tag{4}$$

It is worth mentioning that $\mathrm{p}^{\mathrm{T}}_{t_1}$ and $\mathrm{p}^{\mathrm{T}}_{t_2}$ are not independent, and those can be obtained by $\mathrm{p}^{\mathrm{T}}_{u_1}$ and $\mathrm{p}^{\mathrm{T}}_{u_2}$ with the following Hooke's law:

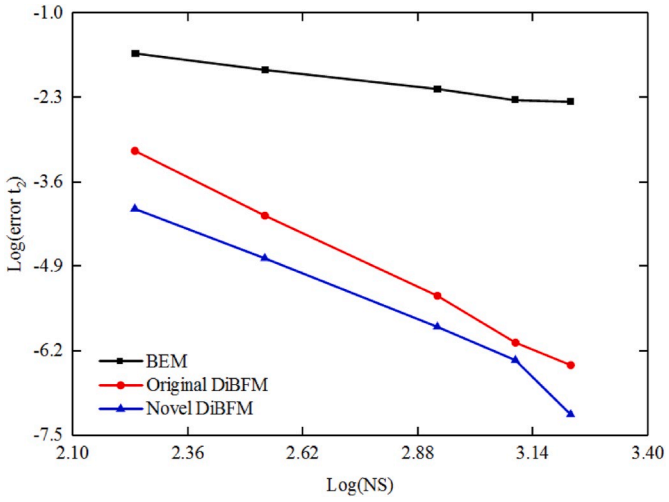

Fig. 6. Comparison of relative errors for traction t_2 obtained by different numerical methods.

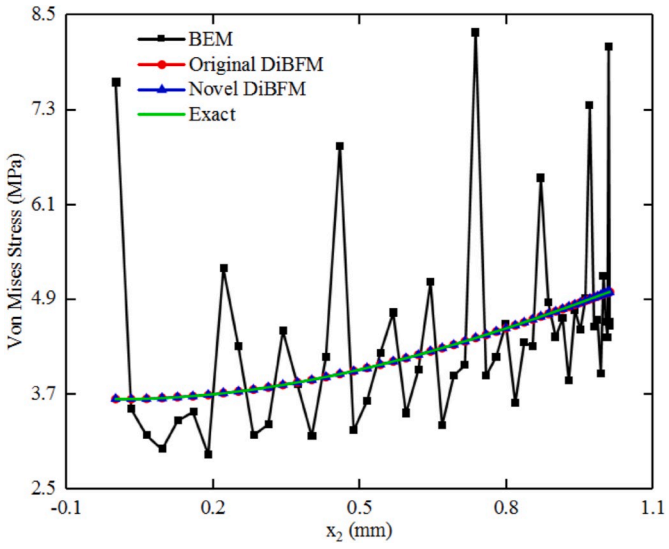

Fig. 7. Comparison of accuracy for Von Mises stress along the curve *AB*.

$$\mathrm{p}^{\mathrm{T}}_{t_i}(x, y, n) = \frac{1}{2} D_{ijkl} \left(\frac{\partial \mathrm{p}^{\mathrm{T}}_{u_k}}{\partial x_l} + \frac{\partial \mathrm{p}^{\mathrm{T}}_{u_l}}{\partial x_k} \right) n_j, \tag{5}$$

where D_{ijkl} is the elastic constitutive tensor and the subscripts $i, j = 1$–2 for 2D elasticity problem.

To compute a_t for the point t, we employ the process of weighted least-square approximation by defining the residual

$$J = \sum_{i}^{2} \sum_{k=1}^{K} w_k(x_t, y_t) \left[\mathrm{p}^{\mathrm{T}}_{u_i}(x_k, y_k) \mathrm{a}_t - u_{ik} \right]^2 + \sum_{i}^{2} \times \sum_{k=1}^{K} w_k(x_t, y_t) \left[\mathrm{p}^{\mathrm{T}}_{t_i}(x_k, y_k, n_k) \mathrm{a}_t - t_{ik} \right]^2, \tag{6}$$

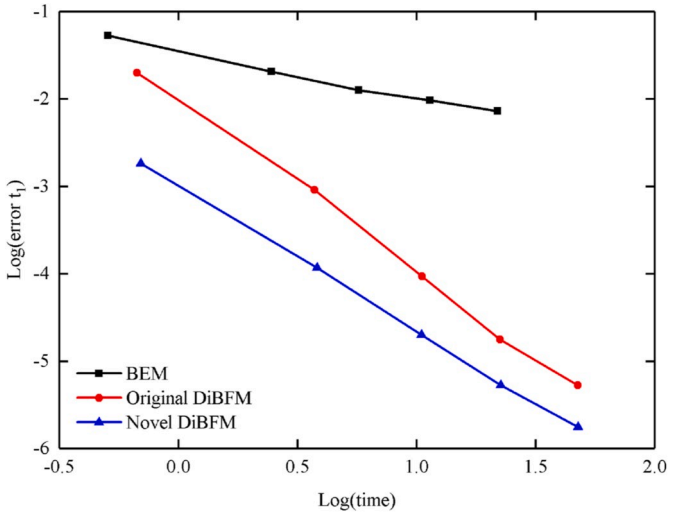

Fig. 8. Comparison of computational efficiency for traction t_1 obtained by different numerical methods.

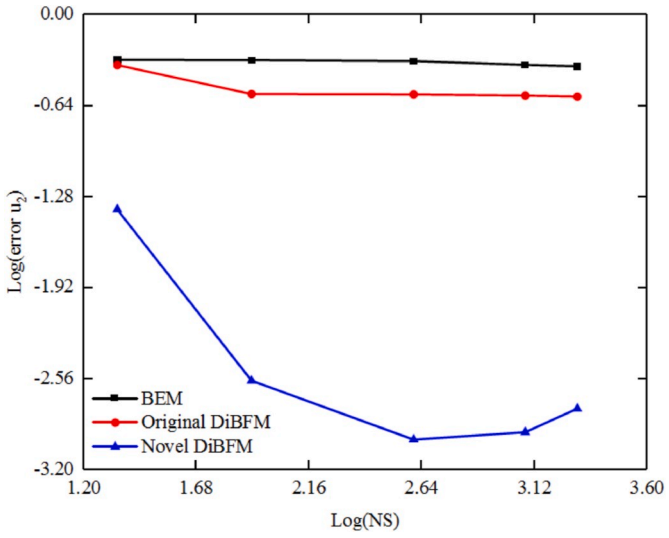

Fig. 10. Comparison of relative errors for displacement u_2 on the long edge AB.

where K is the number of nodes within the vicinity of the point t, and x_k, y_k and n_k are the Cartesian coordinates and unit outward normal at node k, $w_k(x_t, y_t)$ is the weighting function centered at point t, u_{ik} and t_{ik} denote the displacement and traction in i-th direction at node k, respectively.

Minimizing the residual J, we can obtain

$$\left(\sum_{i=1}^{2}\mathbf{P}_{u_i}^{\mathrm{T}}\mathbf{W}\mathbf{P}_{u_i}+\sum_{i=1}^{2}\mathbf{P}_{t_i}^{\mathrm{T}}\mathbf{W}\mathbf{P}_{t_i}\right)\mathbf{a}_t=\sum_{i=1}^{2}\mathbf{P}_{u_i}^{\mathrm{T}}\mathbf{W}\mathbf{u}_i+\sum_{i=1}^{2}\mathbf{P}_{t_i}^{\mathrm{T}}\mathbf{W}\mathbf{t}_i, \tag{7}$$

where $\mathbf{W}$ is $K \times K$ diagonal matrix, $\mathrm{P}_{u_i}^{\mathrm{T}}$ and $\mathrm{P}_{t_i}^{\mathrm{T}}$ are the $m \times K$ matrices, $\mathbf{u}_i$ and $\mathbf{t}_i$ are $K \times 1$ vectors containing displacements and tractions in i-th direction of all nodes, respectively. All matrices are defined as follows:

$$\mathbf{W}=\begin{bmatrix} w_1(x_t,y_t) & 0 & \cdots & 0 \\ 0 & w_2(x_t,y_t) & \cdots & 0 \\ \vdots & \vdots & \ddots & \vdots \\ 0 & 0 & \cdots & w_K(x_t,y_t) \end{bmatrix}_{K\times K}, \tag{8}$$

$$\mathbf{P}_{u_i}^{\mathrm{T}}=\left[\mathbf{p}_{u_i}(x_1,y_1)\mathbf{p}_{u_i}(x_2,y_2)\cdots\mathbf{p}_{u_i}(x_K,y_K)\right], \tag{9}$$

$$\mathbf{P}_{t_i}^{\mathrm{T}}=\left[\mathbf{p}_{t_i}(x_1,y_1,n_1)\mathbf{p}_{t_i}(x_2,y_2,n_2)\cdots\mathbf{p}_{t_i}(x_K,y_K,n_K)\right]. \tag{10}$$

Rewriting Eq. (7), we can obtain

$$\mathrm{C}_t\mathbf{a}_t=\sum_{i=1}^{2}\mathbf{P}_{u_i}^{\mathrm{T}}\mathbf{W}\mathbf{u}_i+\sum_{i=1}^{2}\mathbf{P}_{t_i}^{\mathrm{T}}\mathbf{W}\mathbf{t}_i, \tag{11}$$

$$\mathbf{a}_t=\mathrm{C}_t^{-1}\left(\sum_{i=1}^{2}\mathbf{P}_{u_i}^{\mathrm{T}}\mathbf{W}\mathbf{u}_i+\sum_{i=1}^{2}\mathbf{P}_{t_i}^{\mathrm{T}}\mathbf{W}\mathbf{t}_i\right), \tag{12}$$

with

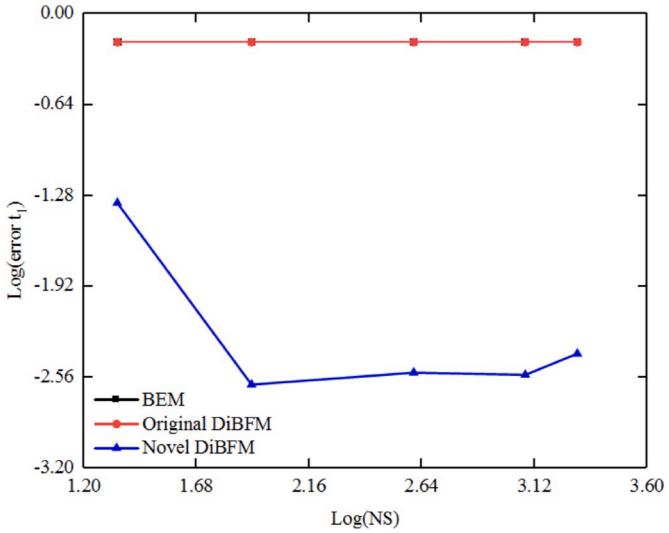

Fig. 11. Comparison of relative errors for traction t_1 on the short edge DA.

$$\mathrm{C}_t=\sum_{i=1}^{2}\mathbf{P}_{u_i}^{\mathrm{T}}\mathbf{W}\mathbf{P}_{u_i}+\sum_{i=1}^{2}\mathbf{P}_{t_i}^{\mathrm{T}}\mathbf{W}\mathbf{P}_{t_i}. \tag{13}$$

Substituting Eq. (12) into (1)~(2) yields:

$$u_i(x,y)=\sum_{j=1}^{2}\boldsymbol{\varphi}^{u_iu_j}(x,y)\mathbf{u}_j+\sum_{j=1}^{2}\boldsymbol{\varphi}^{u_it_j}(x,y)\mathbf{t}_j, \tag{14}$$

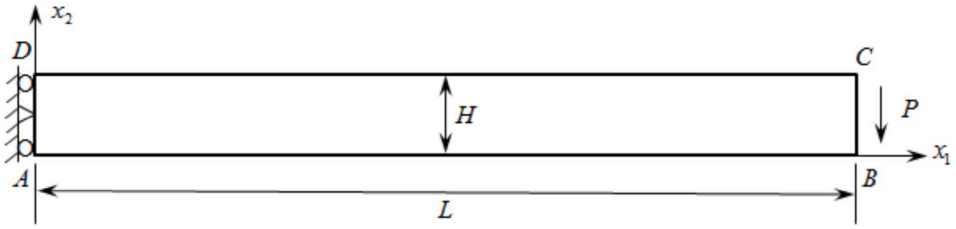

Fig. 9. Cantilever beam problem.

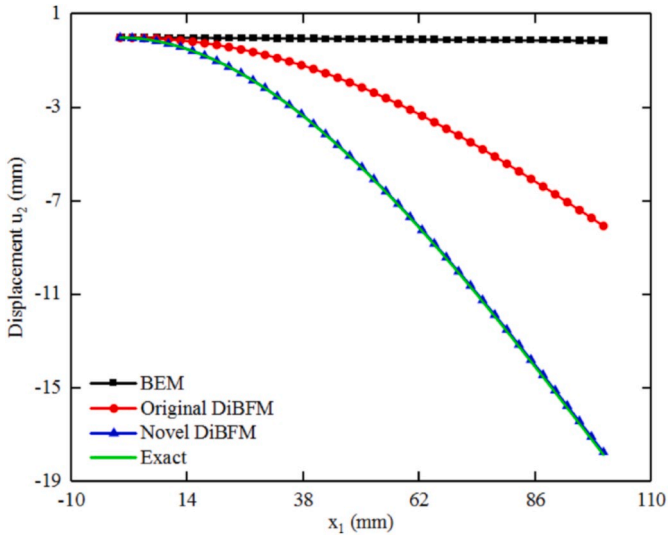

Fig. 12. Comparison of accuracy for displacement u_2 along the long edge AB.

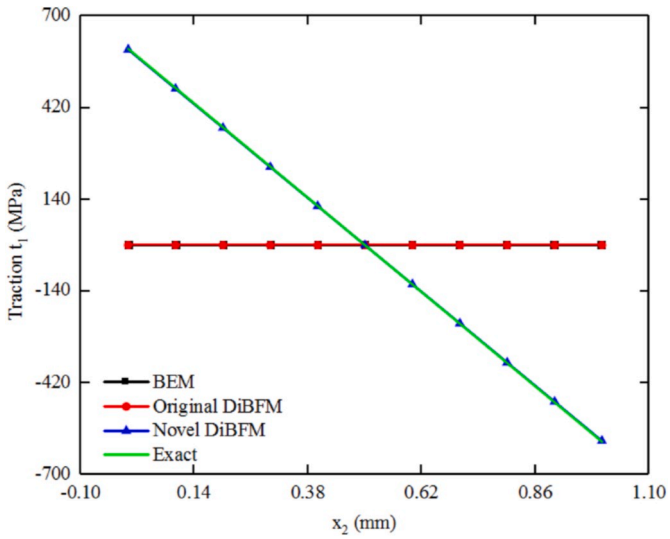

Fig. 13. Comparison of accuracy for traction t_1 along the short edge DA.

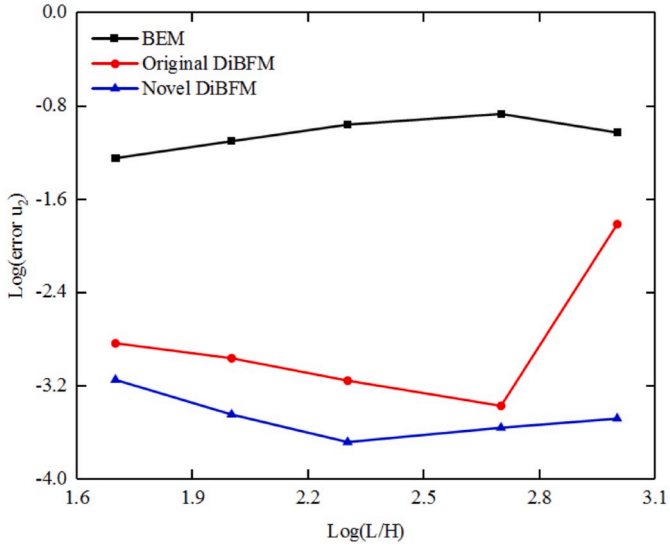

Fig. 14. Comparison of relative errors for displacement u_2 on the long edge AB for $50 \leq L/H \leq 1000$.

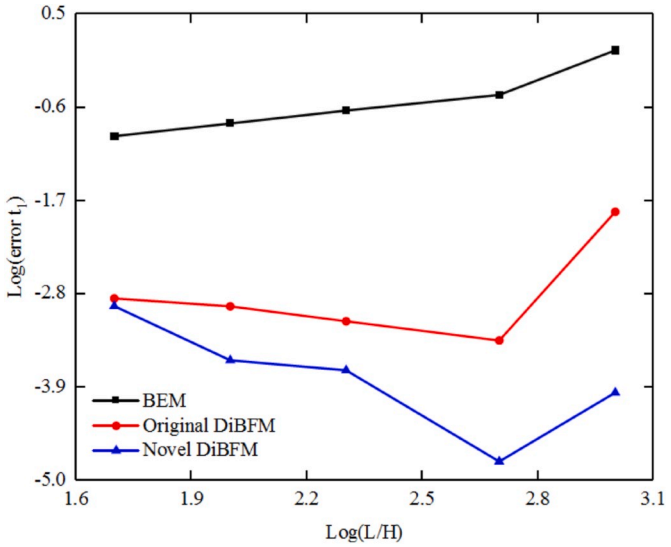

Fig. 15. Comparison of relative errors for t_1 along the short edge DA for $50 \leq L/H \leq 1000$.

$$t_i(x,y,n) = \sum_{j=1}^{2} \boldsymbol{\varphi}^{t_i u_j}(x,y,n)\mathbf{u}_j + \sum_{j=1}^{2} \boldsymbol{\varphi}^{t_i t_j}(x,y,n)\mathbf{t}_j, \tag{15}$$

where $\boldsymbol{\varphi}^{u_i u_j}$, $\boldsymbol{\varphi}^{u_i t_j}$, $\boldsymbol{\varphi}^{t_i u_j}$ and $\boldsymbol{\varphi}^{t_i t_j}$ are $1 \times K$ interpolation vectors formulated by

$$\boldsymbol{\varphi}^{u_i u_j} = \mathbf{p}_{u_i}^{\mathbf{T}}(x,y)\mathbf{C}_t^{-1}\mathbf{P}_{u_j}^{\mathbf{T}}, \tag{16}$$

$$\boldsymbol{\varphi}^{u_i t_j} = \mathbf{p}_{u_i}^{\mathbf{T}}(x,y)\mathbf{C}_t^{-1}\mathbf{P}_{t_j}^{\mathbf{T}}, \tag{17}$$

$$\boldsymbol{\varphi}^{t_i u_j} = \mathbf{p}_{t_i}^{\mathbf{T}}(x,y,n)\mathbf{C}_t^{-1}\mathbf{P}_{u_j}^{\mathbf{T}}, \tag{18}$$

$$\boldsymbol{\varphi}^{t_i t_j} = \mathbf{p}_{t_i}^{\mathbf{T}}(x,y,n)\mathbf{C}_t^{-1}\mathbf{P}_{t_j}^{\mathbf{T}}, \tag{19}$$

where $i, j = 1$–2.

In the proposed method, the shape functions of Hermite-type approximation are with no need to satisfy the delta function property. Therefore, in the all above processes, we directly use the displacements and tractions, rather than fictitious values of them, to perform Hermite-type approximation.

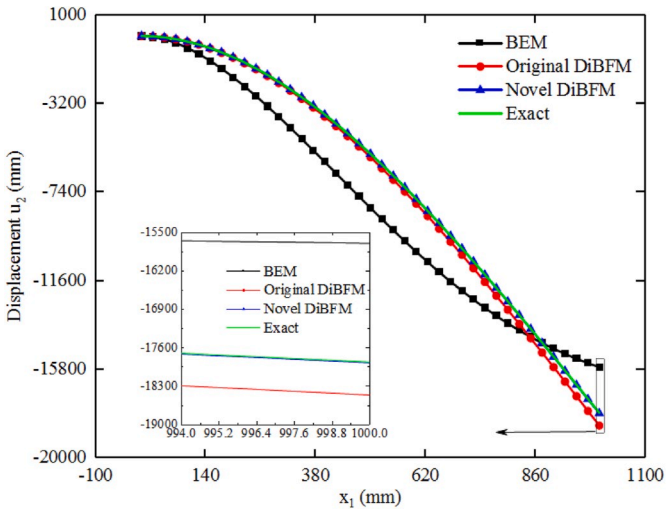

Fig. 16. Comparison of accuracy for displacement u_2 along the long edge AB for $L/H = 1000$.

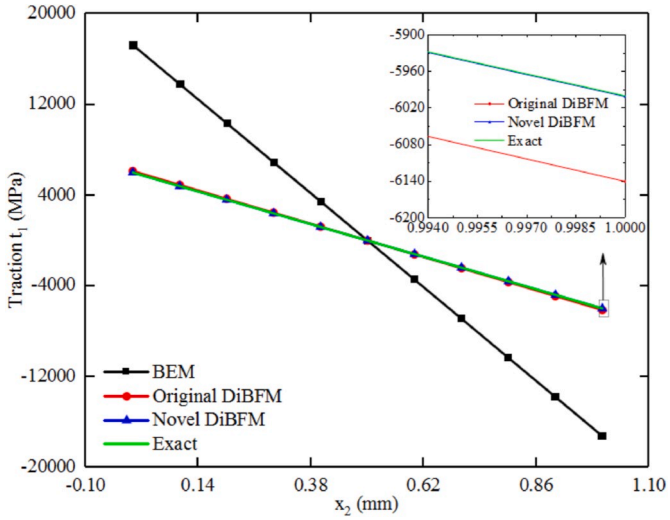

Fig. 17. Comparison of accuracy for traction t_1 along the short edge *DA* for $L/H = 1000$.

3. Dual interpolation method with Hermite-type approximation for elasticity problems

As pointed in (Zhang et al., 2017b, 2019a, 2019b, 2019c), there are two kinds of interpolations in the dual interpolation method. One is the element interpolation, in which the physical variables are interpolated by the source and virtual nodes. The other is meshless approximation, where the physical variables of virtual nodes are approximated by those of source nodes. In this section, the dual interpolation method with Hermite-type approximation for elasticity problems is introduced briefly.

3.1. The first-layer interpolation

For 2D elasticity problems, the independent physical variables on the boundary are the displacements u_i and tractions q_i. In the dual interpolation elements as shown in Fig. 3, those variables are approximated by virtual (v_i) and source (s_i) nodes:

$$u_i(\xi) = \sum_{\alpha=1}^{n\alpha} N_\alpha^s(\xi) u_i(Q_\alpha^s) + \sum_{\beta=1}^{n\beta} N_\beta^v(\xi) u_i(Q_\beta^v), \tag{20}$$

Table 1
The max von Mises stresses in negative Poisson's ratio structure of the novel DiBFM and FEM.

Novel DiBFM			FEM		
NE	NS	*Max_Mises* (MPa)	NE	NS	*Max_Mises* (MPa)
480	1440	356.5	16,974	36,345	336.3
680	2040	352.8	37,116	77,823	343.3
848	2544	353.6	145,464	298,113	357.3
1032	3096	353.4	438,028	888,017	357.6

$$t_i(\xi) = \sum_{\alpha=1}^{n\alpha} N_\alpha^s(\xi) t_i(Q_\alpha^s) + \sum_{\beta=1}^{n\beta} N_\beta^v(\xi) t_i(Q_\beta^v), \tag{21}$$

where $i = 1$–2, ξ is the intrinsic coordinate defined on the element. $n\alpha$ and $n\beta$ are the number of source and virtual nodes of the dual interpolation element, $N_\alpha^s(\xi)$, $u_i(Q_\alpha^s)$ and $t_i(Q_\alpha^s)$ are the shape functions, displacements and tractions in the *i-th* direction of the α^{th} source node in dual interpolation element, $N_\beta^v(\xi)$, $u_i(Q_\beta^v)$ and $q_i(Q_\beta^v)$ are the shape functions, displacements and tractions in the *i-th* direction of the β^{th} virtual node in dual interpolation element, respectively. In this method, the variables $u_i(Q_\beta^v)$ and $q_i(Q_\beta^v)$ are not independent and can be determined by the Hermite-type approximation.

3.2. The second-layer interpolation

In this paper, we employ Hermite-type approximation as the second-layer interpolation, which is used to obtain the relationships for physical variables of virtual and source nodes.

According to Eqs. (14)~(15) in section 2, the values of the unknown displacement u_i and traction t_i of virtual node Q_β^v are approximated by the Hermite-type approximation as follows:

$$u_i(Q_\beta^v) = \sum_{j=1}^{2} \sum_{k=1}^{K} \varphi_k^{u_i u_j}(x^v, y^v) u_j(Q_k^s) + \sum_{j=1}^{2} \sum_{k=1}^{K} \varphi_k^{u_i t_j}(x^v, y^v) t_j(Q_k^s), \tag{22}$$

$$t_i(Q_\beta^v) = \sum_{j=1}^{2} \sum_{k=1}^{K} \varphi_k^{t_i u_j}(x^v, y^v, n^v) u_j(Q_k^s) + \sum_{j=1}^{2} \sum_{k=1}^{K} \varphi_k^{t_i t_j}(x^v, y^v, n^v) t_j(Q_k^s), \tag{23}$$

where $i = 1$–2, K is the number of source nodes located in the vicinity of the virtual node Q_β^v. $u_j(Q_k^s)$ and $t_j(Q_k^s)$ are the values of displacement and traction in the *j-th* direction at source nodal Q_k^s, the terms (x^v, y^v) and n^v

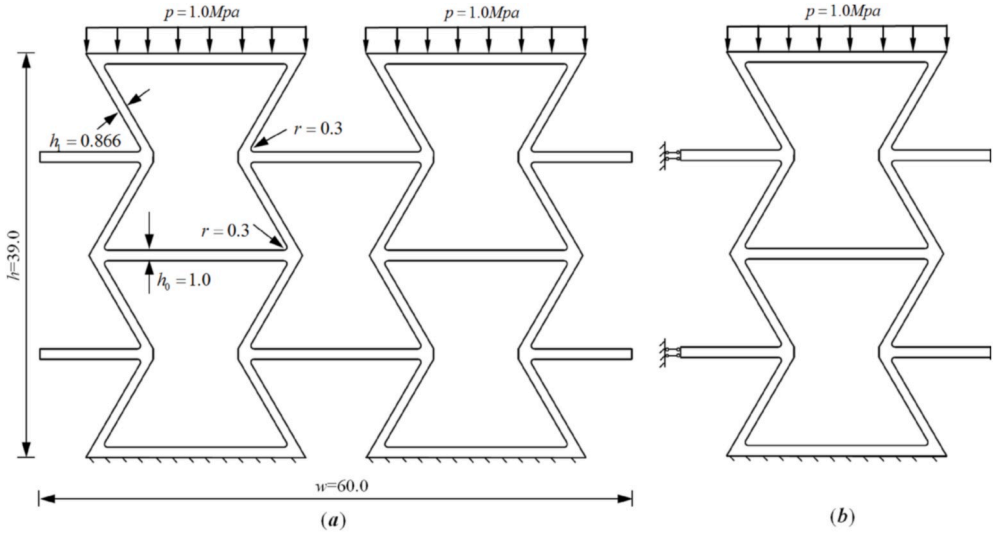

Fig. 18. A negative Poisson's ratio structure with small features compressed by a uniform pressure: (a) geometry and boundary condition for the whole structure, (b) half of computational model based on the symmetry of the problem.

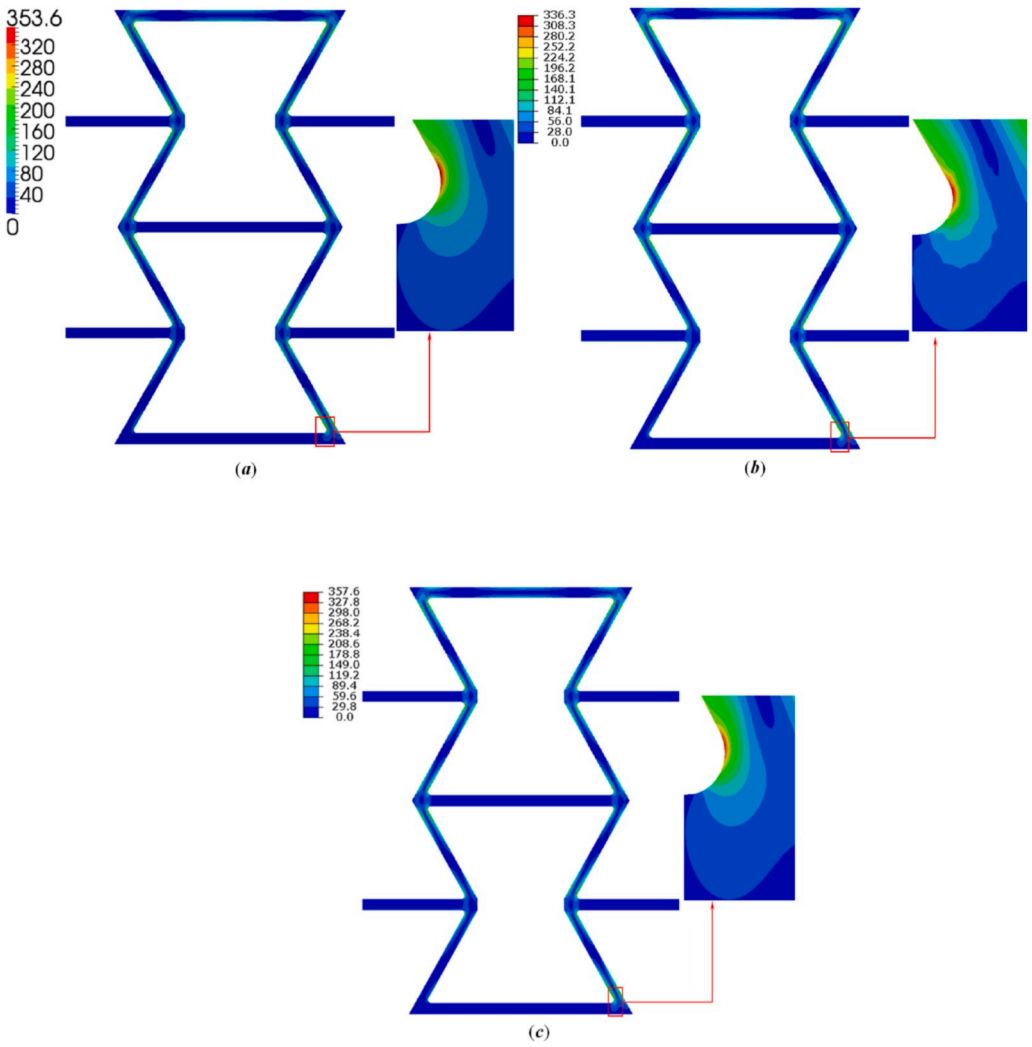

Fig. 19. The von Mises stress distributions: (a) novel DiBFM with 2544 source points, (b) FEM with 36,345 nodes, (c) FEM with 888,017 nodes.

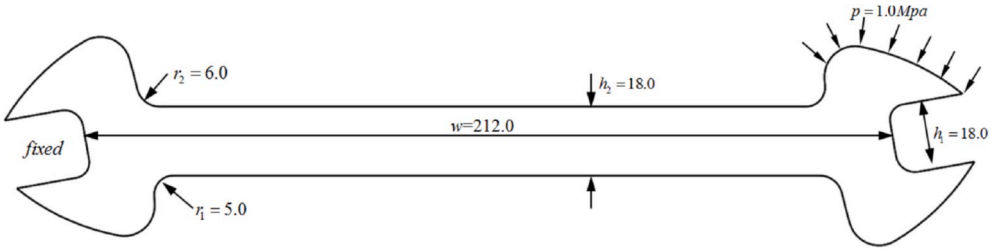

Fig. 20. A spanner subjected to a uniform compressive stress on the right side: geometric model and boundary conditions.

Table 2
The max von Mises stresses in the spanner obtained by the novel DiBFM and FEM.

Novel DiBFM			FEM		
NE	NS	*Max_Mises* (MPa)	NE	NS	*Max_Mises* (MPa)
246	738	198.2	2900	6139	189.6
306	918	197.5	5222	10,897	195.6
437	1311	197.5	126,764	255,789	199.0
500	1500	197.6	318,504	640,395	198.8

are the Cartesian coordinates and outward normal at virtual node Q_β^v, respectively. Furthermore, $\varphi_k^{u_i u_j}(x^v, y^v)$, $\varphi_k^{u_i t_j}(x^v, y^v)$, $\varphi_k^{t_i u_j}(x^v, y^v, n^v)$, are the shape functions of Hermite-type approximation corresponding to the *k-th* component of interpolation vectors in Eqs. (16)~(19).

4. DiBFM with Hermite-type approximation for elasticity problems

In this section, the boundary integral equation for elasticity problems and its discretization are introduced. Moreover, the procedure of condensing degrees of freedom of the virtual nodes will be described in

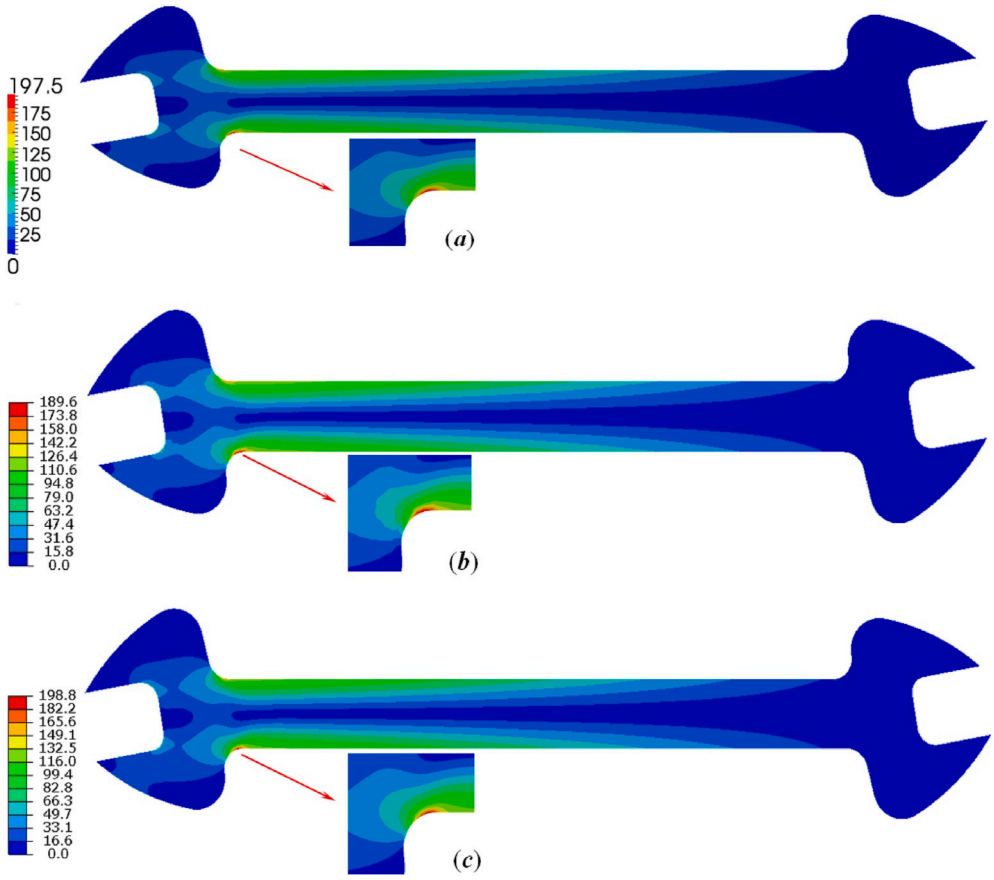

Fig. 21. Contour plots of von Mises stress in the spanner: (a) novel DiBFM with 918 source points, (b) FEM with 6139 source points, (c) FEM with 640,395 nodes.

detail.

4.1. Boundary integral equation

The well-known boundary integral equation (BIE) for the elasticity problems in 2D with a finite region Ω bounded by a boundary Γ is

$$c_{ij}(P)u_j(P) = \int_\Gamma U_{ij}(P,Q)t_j(Q)d\Gamma(Q) - \int_\Gamma T_{ij}(P,Q)u_j(Q)d\Gamma(Q), \qquad P,Q \in \Gamma, \tag{24}$$

where $i, j = 1$–2 for 2D elasticity problems, u_j and t_j are the displacement and traction components, respectively. The coefficient $c_{ij}(P) = 1/2\delta_{ij}$, when Γ is smooth at source node P. $U_{ij}(P,Q)$ and $T_{ij}(P,Q)$ are fundamental solutions. For plane-strain problems, they are given by

$$U_{ij}(P,Q) = \frac{1}{8\pi\mu(1-\nu)}\left[(3-4\nu)\delta_{ij}\ln\frac{1}{r} + r_{,i}r_{,j}\right], \tag{25}$$

$$T_{ij}(P,Q) = -\frac{1}{4\pi(1-\nu)r}\left\{\frac{\partial r}{\partial n}\left[(1-2\nu)\delta_{ij} + 2r_{,i}r_{,j}\right] - (1-2\nu)\left(r_{,i}n_j - r_{,j}n_i\right)\right\}, \tag{26}$$

where r is the Euclidean distance between the source node P and field point Q, n is the unit outward normal at field point Q, n_i and n_j are the components of n, μ and ν are the shear modulus and the Poisson's ratio, respectively.

4.2. Discretization of the BIE for elasticity problems

In the DiBFM, the BIE is discretized by the dual interpolation elements. The numbers of elements, source nodes, virtual nodes, and field nodes are denoted *NE*, *NS*, *NV*, and *NM*, respectively. As mentioned earlier, the boundary integral equations are only collocated at the source node P_k ($k = 1, 2, \ldots, NS$). Thus, the discretization form of Eq. (24) can be written as

$$\sum_{e=1}^{NE}\left[\sum_{\alpha=1}^{n\alpha} h_{ij}^{ss}(P_k)u_j\left(Q_{e(\alpha)}^s\right) + \sum_{\beta=1}^{n\beta} h_{ij}^{sv}(P_k)u_j\left(Q_{e(\beta)}^v\right)\right] = \sum_{e=1}^{NE}\left[\sum_{\alpha=1}^{n\alpha} g_{ij}^{ss}(P_k)t_j\left(Q_{e(\alpha)}^s\right) + \sum_{\beta=1}^{n\beta} g_{ij}^{sv}(P_k)t_j\left(Q_{e(\beta)}^v\right)\right], \tag{27}$$

with

$$h_{ij}^{ss}(P_k) = \int_{\Gamma_e} T_{ij}(P_k,Q)N_{e(\alpha)}^s(Q)d\Gamma_e(Q) + \frac{1}{2}\delta_{ij}\delta_{e(\alpha)}^k, \tag{28}$$

$$h_{ij}^{sv}(P_k) = \int_{\Gamma_e} T_{ij}(P_k,Q)N_{e(\beta)}^v(Q)d\Gamma_e(Q), \tag{29}$$

$$g_{ij}^{ss}(P_k)=\int_{\Gamma_e}U_{ij}(P_k,Q)N_{e(\alpha)}^{s}(Q)d\Gamma_e(Q), \tag{30}$$

$$g_{ij}^{sv}(P_k)=\int_{\Gamma_e}U_{ij}(P_k,Q)N_{e(\beta)}^{v}(Q)d\Gamma_e(Q), \tag{31}$$

and

$$\delta_{e(\alpha)}^{k}=\begin{cases}1, & \text{if source node } P_k \text{ is the } \alpha^{\text{th}} \text{ source node in the } e^{\text{th}} \text{ element}\\ 0,\end{cases} \tag{32}$$

where Γ_e denotes the boundary of domain corresponding to eth element, $N_{e(\alpha)}^{s}$, $u_j(Q_{e(\alpha)}^{s})$ and $t_j(Q_{e(\alpha)}^{s})$ are the shape function, displacement and traction of α^{th} source node in eth element, $N_{e(\beta)}^{v}$, $u_j(Q_{e(\beta)}^{v})$ and $t_j(Q_{e(\beta)}^{v})$ are the shape function, displacement and traction of β^{th} virtual node in eth element, respectively.

The matrix form of Eq. (27) is

$$\begin{bmatrix}\mathbf{H}_{11}^{ss} & \mathbf{H}_{12}^{ss}\\ \mathbf{H}_{21}^{ss} & \mathbf{H}_{22}^{ss}\end{bmatrix}\begin{Bmatrix}\mathbf{u}_1^{s}\\ \mathbf{u}_2^{s}\end{Bmatrix}+\begin{bmatrix}\mathbf{H}_{11}^{sv} & \mathbf{H}_{12}^{sv}\\ \mathbf{H}_{21}^{sv} & \mathbf{H}_{22}^{sv}\end{bmatrix}\begin{Bmatrix}\mathbf{u}_1^{v}\\ \mathbf{u}_2^{v}\end{Bmatrix}=\begin{bmatrix}\mathbf{G}_{11}^{ss} & \mathbf{G}_{12}^{ss}\\ \mathbf{G}_{21}^{ss} & \mathbf{G}_{22}^{ss}\end{bmatrix}\begin{Bmatrix}\mathbf{t}_1^{s}\\ \mathbf{t}_2^{s}\end{Bmatrix}+\begin{bmatrix}\mathbf{G}_{11}^{sv} & \mathbf{G}_{12}^{sv}\\ \mathbf{G}_{21}^{sv} & \mathbf{G}_{22}^{sv}\end{bmatrix}\begin{Bmatrix}\mathbf{t}_1^{v}\\ \mathbf{t}_2^{v}\end{Bmatrix}, \tag{33}$$

where $\mathbf{H}_{ij}^{ss}$ and $\mathbf{G}_{ij}^{ss}$ are $NS\times NS$ coefficient matrices, $\mathbf{H}_{ij}^{sv}$ and $\mathbf{G}_{ij}^{sv}$ are $NS\times NV$ coefficient matrices, $\mathbf{u}_i^{s}$ and $\mathbf{t}_i^{s}$ are vectors of NS components containing the i-th direction displacement and traction of all source nodes, $\mathbf{u}_i^{v}$ and $\mathbf{t}_i^{v}$ are vectors of NV components containing the i-th direction displacement and traction of all virtual nodes, respectively.

As we can see, the coefficient matrices in Eq. (33) are not square matrices. Thus, the degrees of freedom relating to all virtual nodes should be condensed by the second-layer interpolation which is proposed in section 3.2.

4.3. Condensation of degrees of freedom for virtual nodes

The vectors $\mathbf{u}_i^{v}$ and $\mathbf{t}_i^{v}$ contain known and unknown variables, so these vectors can be recast into the following form

$$\mathbf{u}_i^{v}=\overline{\mathbf{u}}_i^{v}+\widehat{\mathbf{u}}_i^{v}, \tag{34}$$

$$\mathbf{t}_i^{v}=\overline{\mathbf{t}}_i^{v}+\widehat{\mathbf{t}}_i^{v}, \tag{35}$$

where $\overline{\mathbf{u}}_i^{v}$, $\widehat{\mathbf{u}}_i^{v}$, $\overline{\mathbf{t}}_i^{v}$, and $\widehat{\mathbf{t}}_i^{v}$ are $NV\times 1$ vectors involving the known and unknown displacements and tractions of the virtual nodes, respectively.

For each virtual node, the values of the unknown displacement and traction in $\widehat{\mathbf{u}}_i^{v}$ and $\widehat{\mathbf{t}}_i^{v}$ can be approximated by the Hermite-type approximation defined in Eqs. (22)~(23). Thus, $\widehat{\mathbf{u}}_i^{v}$ and $\widehat{\mathbf{t}}_i^{v}$ are expressed as

$$\widehat{\mathbf{u}}_i^{v}=\mathbf{\Phi}_{u_iu_j}^{vs}\mathbf{u}_j^{s}+\mathbf{\Phi}_{u_it_j}^{vs}\mathbf{t}_j^{s}, \tag{36}$$

$$\widehat{\mathbf{t}}_i^{v}=\mathbf{\Phi}_{t_iu_j}^{vs}\mathbf{u}_j^{s}+\mathbf{\Phi}_{t_it_j}^{vs}\mathbf{t}_j^{s}, \tag{37}$$

where $\mathbf{\Phi}_{u_iu_j}^{vs}$, $\mathbf{\Phi}_{u_it_j}^{vs}$, $\mathbf{\Phi}_{t_iu_j}^{vs}$ and $\mathbf{\Phi}_{t_it_j}^{vs}$ are shape function matrices which can be obtained by the Hermite-type approximation presented in section 2.

Substituting Eqs. (34)~(37) into (33), we can obtain:

$$\begin{bmatrix}\overline{\mathbf{H}}_{11}^{ss} & \overline{\mathbf{H}}_{12}^{ss}\\ \overline{\mathbf{H}}_{21}^{ss} & \overline{\mathbf{H}}_{22}^{ss}\end{bmatrix}\begin{Bmatrix}\mathbf{u}_1^{s}\\ \mathbf{u}_2^{s}\end{Bmatrix}=\begin{bmatrix}\overline{\mathbf{G}}_{11}^{ss} & \overline{\mathbf{G}}_{12}^{ss}\\ \overline{\mathbf{G}}_{21}^{ss} & \overline{\mathbf{G}}_{22}^{ss}\end{bmatrix}\begin{Bmatrix}\mathbf{t}_1^{s}\\ \mathbf{t}_2^{s}\end{Bmatrix}+\begin{bmatrix}\mathbf{G}_{11}^{sv} & \mathbf{G}_{12}^{sv}\\ \mathbf{G}_{21}^{sv} & \mathbf{G}_{22}^{sv}\end{bmatrix}\begin{Bmatrix}\overline{\mathbf{t}}_1^{v}\\ \overline{\mathbf{t}}_2^{v}\end{Bmatrix}-\begin{bmatrix}\mathbf{H}_{11}^{sv} & \mathbf{H}_{12}^{sv}\\ \mathbf{H}_{21}^{sv} & \mathbf{H}_{22}^{sv}\end{bmatrix}\begin{Bmatrix}\overline{\mathbf{u}}_1^{v}\\ \overline{\mathbf{u}}_2^{v}\end{Bmatrix}, \tag{38}$$

with

$$\begin{bmatrix}\overline{\mathbf{H}}_{11}^{ss} & \overline{\mathbf{H}}_{12}^{ss}\\ \overline{\mathbf{H}}_{21}^{ss} & \overline{\mathbf{H}}_{22}^{ss}\end{bmatrix}=\begin{bmatrix}\mathbf{H}_{11}^{ss} & \mathbf{H}_{12}^{ss}\\ \mathbf{H}_{21}^{ss} & \mathbf{H}_{22}^{ss}\end{bmatrix}+\begin{bmatrix}\mathbf{H}_{11}^{sv} & \mathbf{H}_{12}^{sv}\\ \mathbf{H}_{21}^{sv} & \mathbf{H}_{22}^{sv}\end{bmatrix}\begin{bmatrix}\mathbf{\Phi}_{u_1u_1}^{vs} & \mathbf{\Phi}_{u_1u_2}^{vs}\\ \mathbf{\Phi}_{u_2u_1}^{vs} & \mathbf{\Phi}_{u_2u_2}^{vs}\end{bmatrix}-\begin{bmatrix}\mathbf{G}_{11}^{sv} & \mathbf{G}_{12}^{sv}\\ \mathbf{G}_{21}^{sv} & \mathbf{G}_{22}^{sv}\end{bmatrix}\begin{bmatrix}\mathbf{\Phi}_{t_1u_1}^{vs} & \mathbf{\Phi}_{t_1u_2}^{vs}\\ \mathbf{\Phi}_{t_2u_1}^{vs} & \mathbf{\Phi}_{t_2u_2}^{vs}\end{bmatrix} \tag{39}$$

and

$$\begin{bmatrix}\overline{\mathbf{G}}_{11}^{ss} & \overline{\mathbf{G}}_{12}^{ss}\\ \overline{\mathbf{G}}_{21}^{ss} & \overline{\mathbf{G}}_{22}^{ss}\end{bmatrix}=\begin{bmatrix}\mathbf{G}_{11}^{ss} & \mathbf{G}_{12}^{ss}\\ \mathbf{G}_{21}^{ss} & \mathbf{G}_{22}^{ss}\end{bmatrix}+\begin{bmatrix}\mathbf{G}_{11}^{sv} & \mathbf{G}_{12}^{sv}\\ \mathbf{G}_{21}^{sv} & \mathbf{G}_{22}^{sv}\end{bmatrix}\begin{bmatrix}\mathbf{\Phi}_{t_1t_1}^{vs} & \mathbf{\Phi}_{t_1t_2}^{vs}\\ \mathbf{\Phi}_{t_2t_1}^{vs} & \mathbf{\Phi}_{t_2t_2}^{vs}\end{bmatrix}-\begin{bmatrix}\mathbf{H}_{11}^{sv} & \mathbf{H}_{12}^{sv}\\ \mathbf{H}_{21}^{sv} & \mathbf{H}_{22}^{sv}\end{bmatrix}\begin{bmatrix}\mathbf{\Phi}_{u_1t_1}^{vs} & \mathbf{\Phi}_{u_1t_2}^{vs}\\ \mathbf{\Phi}_{u_2t_1}^{vs} & \mathbf{\Phi}_{u_2t_2}^{vs}\end{bmatrix}. \tag{40}$$

Considering the boundary conditions imposed on source points, the vectors $\mathbf{u}_i^{s}$ and $\mathbf{t}_i^{s}$ contain known and unknown variables. Thus, Eq. (38) can be recast into

$$\begin{bmatrix}\overline{\mathbf{H}}_{11}^{ss} & \overline{\mathbf{H}}_{12}^{ss}\\ \overline{\mathbf{H}}_{21}^{ss} & \overline{\mathbf{H}}_{22}^{ss}\end{bmatrix}\begin{Bmatrix}\widehat{\mathbf{u}}_1^{s}\\ \widehat{\mathbf{u}}_2^{s}\end{Bmatrix}=\begin{bmatrix}\overline{\mathbf{G}}_{11}^{ss} & \overline{\mathbf{G}}_{12}^{ss}\\ \overline{\mathbf{G}}_{21}^{ss} & \overline{\mathbf{G}}_{22}^{ss}\end{bmatrix}\begin{Bmatrix}\widehat{\mathbf{t}}_1^{s}\\ \widehat{\mathbf{t}}_2^{s}\end{Bmatrix}+\begin{Bmatrix}\overline{\mathbf{b}}_1\\ \overline{\mathbf{b}}_2\end{Bmatrix}, \tag{41}$$

with

$$\begin{Bmatrix}\overline{\mathbf{b}}_1\\ \overline{\mathbf{b}}_2\end{Bmatrix}=\begin{bmatrix}\overline{\mathbf{G}}_{11}^{ss} & \overline{\mathbf{G}}_{12}^{ss}\\ \overline{\mathbf{G}}_{21}^{ss} & \overline{\mathbf{G}}_{22}^{ss}\end{bmatrix}\begin{Bmatrix}\overline{\mathbf{t}}_1^{s}\\ \overline{\mathbf{t}}_2^{s}\end{Bmatrix}-\begin{bmatrix}\overline{\mathbf{H}}_{11}^{ss} & \overline{\mathbf{H}}_{12}^{ss}\\ \overline{\mathbf{H}}_{21}^{ss} & \overline{\mathbf{H}}_{22}^{ss}\end{bmatrix}\begin{Bmatrix}\overline{\mathbf{u}}_1^{s}\\ \overline{\mathbf{u}}_2^{s}\end{Bmatrix}+\begin{bmatrix}\mathbf{G}_{11}^{sv} & \mathbf{G}_{12}^{sv}\\ \mathbf{G}_{21}^{sv} & \mathbf{G}_{22}^{sv}\end{bmatrix}\begin{Bmatrix}\overline{\mathbf{t}}_1^{v}\\ \overline{\mathbf{t}}_2^{v}\end{Bmatrix}-\begin{bmatrix}\mathbf{H}_{11}^{sv} & \mathbf{H}_{12}^{sv}\\ \mathbf{H}_{21}^{sv} & \mathbf{H}_{22}^{sv}\end{bmatrix}\begin{Bmatrix}\overline{\mathbf{u}}_1^{v}\\ \overline{\mathbf{u}}_2^{v}\end{Bmatrix}, \tag{42}$$

where $\overline{\mathbf{u}}_i^{s}$, $\widehat{\mathbf{u}}_i^{s}$, $\overline{\mathbf{t}}_i^{s}$, and $\widehat{\mathbf{t}}_i^{s}$ are the known and unknown displacements and tractions vectors about source nodes, respectively.

Finally, the solvable system of linear equations can be obtained from Eq. (41)

$$\mathbf{A}\mathbf{x}=\mathbf{b}, \tag{43}$$

where

$$\mathbf{A}=\begin{bmatrix}\overline{\mathbf{H}}_{11}^{ss} & \overline{\mathbf{H}}_{12}^{ss} & \overline{\mathbf{G}}_{11}^{ss} & \overline{\mathbf{G}}_{12}^{ss}\\ \overline{\mathbf{H}}_{21}^{ss} & \overline{\mathbf{H}}_{22}^{ss} & \overline{\mathbf{G}}_{21}^{ss} & \overline{\mathbf{G}}_{22}^{ss}\end{bmatrix},\ \mathbf{x}=\begin{Bmatrix}\widehat{\mathbf{u}}_1^{s}\\ \widehat{\mathbf{u}}_2^{s}\\ \widehat{\mathbf{t}}_1^{s}\\ \widehat{\mathbf{t}}_2^{s}\end{Bmatrix},\ \text{and}\ \mathbf{b}=\begin{Bmatrix}\overline{\mathbf{b}}_1\\ \overline{\mathbf{b}}_2\end{Bmatrix},$$

where $\mathbf{A}$ is a $4\times NS\times NS$ coefficient matrix, $\mathbf{x}$ is a $NS\times 2$ boundary unknowns vector only involving source nodes, and $\mathbf{b}$ is a $NS\times 2$ known vector.

The size of Eq. (43) is identical to that in the traditional BEM with discontinuous element, while the novel DiBFM can achieve higher accuracy by improving interpolation accuracy of boundary element.

5. Numerical examples

In this section, four numerical examples are presented to testify the validity of our method for solving the 2D elasticity problems. The first example is given to show the accuracy and efficiency. The second example is a cantilever beam which is used to demonstrate the capability to deal with thin-wall structure. The last two examples are negative Poisson's ratio structure with small features and a spanner, which testify the ability and practicability of our method to handle real-world complex structures.

The error estimation and convergence are measured by the relative error defined as

$$error = \frac{1}{|v^{(e)}|_{\max}} \sqrt{\frac{1}{M}\sum_{i=1}^{M}\left[v_i^{(e)} - v_i^{(n)}\right]^2}, \tag{44}$$

where $|v^{(e)}|_{\max}$ is the maximum value of exact solution over M sample points, the superscripts (e) and (n) denote the exact and computational solutions, respectively. In the following examples, symbol *Max_Mises* denote the max von Mises stresses in structure.

5.1. Dirichlet problem on regular hexagon with circle

The first example is a Dirichlet problem on regular hexagon with circle. The dimensions of the structure are shown in Fig. 4 and Dirichlet boundary conditions are specified along all edges of the boundary. The analytical solution for this problem is given by

$$\begin{cases} u_1 = x_2^3 - 3x_1^2x_2 + x_1 + 0.5x_2 \\ u_2 = -x_1^3 + 3x_1x_2^2 + x_2 + 0.5x_1 \end{cases}. \tag{45}$$

This example is presented to show the accuracy and efficiency of the proposed method compared with results obtained by the original DiBFM and traditional BEM. The problem is analyzed under plane strain conditions with Young's modulus $E = 1.0Mpa$ and Poisson's ratio $v = 0.25$. We employ five sets of source nodes from 174 to 1680 to study the accuracy and efficiency of the proposed method. The S1 elements are employed to approximate displacements and tractions in our method and the original DiBFM, while constant elements are used in conventional BEM. The relative errors for t_1 and t_2 with different methods are plotted in Fig. 5 and Fig. 6. Numerical and exact results of the Von Mises stress along the curve AB with 342 source nodes are plotted in Fig. 7. Moreover, the relative errors of t_1 with CPU time are shown in Fig. 8. As we can see from all the results, with the same number of source points, our method can obtain higher accuracy and efficiency than those by the original DiBFM and traditional BEM.

5.2. Cantilever beam

To show the advantages of the proposed method to solve the slender and thin-wall structure, a cantilever beam subjected to shear force is presented. The dimensions and boundary condition are shown in Fig. 9, where L and H are the length and width of cantilever, respectively. The analytical solutions of this problem are:

$$\begin{cases} u_1 = -\dfrac{P}{6\overline{E}I}\left(x_2 - \dfrac{H}{2}\right)\left[(6L - 3x_1)x_1 + (2+\overline{v})\left(x_2^2 - 2Hx_2\right)\right] \\ u_2 = \dfrac{P}{6\overline{E}I}\left[3\overline{v}\left(x_2^2 - 2Hx_2 + \dfrac{1}{2}H^2\right)(L - x_1) + \dfrac{1}{4}(4+5\overline{v})H^2x_1 + \left(L - \dfrac{1}{3}x_1\right)3x_1^2\right] \end{cases}, \tag{46}$$

and

$$\begin{cases} \sigma_{11} = -\dfrac{P}{I}(L - x_1)\left(x_2 - \dfrac{H}{2}\right) \\ \sigma_{22} = 0 \\ \sigma_{12} = -\dfrac{Px_2}{2I}(x_2 - H) \end{cases}, \tag{47}$$

where

$$I = \frac{H^3}{12},$$

$$\overline{E} = \begin{cases} E \text{ for plane stress} \\ E/(1 - v^2) \text{ for plane strain} \end{cases},$$

$$\overline{v} = \begin{cases} v \text{ for plane stress} \\ v/(1 - v) \text{ for plane strain} \end{cases}.$$

The problem is solved under plane strain case with $P = 1.0$ MPa, $E = 210.0$ GPa, $v = 0.25$. In this example, we first adopt five sets of source points from 22 to 2002 to study the accuracy and convergence of the proposed method in disposing the thin-wall structure of $L = 100.0$ mm and $H = 1.0$ mm. The linear elements are used to approximate the physical variables on edges AB and CD. It should be noted that only one constant element is allocated on the short edges DA and BC, respectively. Then, we employ five sets of L/H from 50 to 1000 to research the performance of the proposed method in handling thin-wall structures. In this case, we allocate only one linear element on short edges and 100 quadratic elements on long edges, respectively.

With the increasing number of source points, the relative errors for u_2 on edge AB and t_1 on edge DA are shown in Fig. 10 and Fig. 11, respectively. Moreover, the values of u_2 on edge AB and t_1 on edge DA obtained by our method using 82 source points are presented in Fig. 12 and Fig. 13, together with results obtained by exact solutions, the original DiBFM and classical BEM. As shown in Figs. 10–13, the accuracy of results obtained by the conventional BEM and original DiBFM hardly improve with the increasing number of source points on edge AB, especially for traction t_1 on edge DA. However, those are largely enhanced in the proposed method. This is mainly due to the fact that it cannot construct the second-layer interpolation at virtual nodes located at the end of edge DA in the original DiBFM, while it can be done in the presented method. As a result, in other two contrastive methods, the physical variables on short edges are essentially approximated by constant element, while quadratic interpolation order can be achieved in our method.

Additionally, Fig. 14 and Fig. 15 present the relative errors of displacement u_2 on the long edge AB and traction t_1 on the short edge DA in $50 \le L/H \le 1000$; Fig. 16 and Fig. 17 show the comparisons of accuracy for displacement u_2 and traction t_1 in $L/H = 1000$, respectively. As it may be observed, with the increasing value of L/H, the errors of displacement u_2 and traction t_1 in the BEM increase and the accuracy is always low. The original DiBFM is better than the BEM, but it yields unsatisfactory results for $L/H = 1000$. However, our method is always better than the other two numerical methods and provides an acceptable engineering accuracy, even for $L/H = 1000$.

5.3. Negative Poisson's ratio structure with small features

The third example is a negative Poisson's ratio structure with small features compressed by a uniform pressure $p = 1.0Mpa$. The dimensions and imposed boundary conditions are shown in Fig. 18 (a). Due to the symmetry of the problem, only one half of the model given in Fig. 18 (b) is analyzed. The material with Young's modulus $E = 200.0Gpa$ and Poisson's ratio $v = 0.25$ is assumed and this problem is analyzed under plane stress condition. Displacements and tractions on the boundary are all approximated by S3 elements. To testify the ability of our method for disposing structures with small features where local stress concentrations maybe occur, the results obtained by FEM with quadratic triangle elements are taken as reference solutions.

The max von Mises stresses with increasing number of source points are listed in Table 1. And the von Mises stress distributions in whole domain are displayed in Fig. 19. From the table and figures, the convergence value of max von Mises stress of this problem obtained by our method is within 1.2% of value obtained by FEM. This example illustrates that our method is capable of solving thin-walled structures with small features and simulating local stress concentration.

5.4. Spanner

To verify the practicability of the proposed method to handle complex engineering structure, we consider a spanner whose dimensions are given in Fig. 20. The right side of the specimen is subjected to a uniform compressive stress in the direction perpendicular to the boundary, and the left notch is fixed. This problem is analyzed under plane stress

conditions with Young's modules $E = 210.0$ GPa and Poisson's ratio $\nu = 0.25$. All physical variables are also approximated by S3 elements and the results obtained by FEM with 640,395 nodes are employed as reference solutions.

Four sets of max von Mises stresses obtained by both the novel DiBFM and FEM are listed in Table 2. Moreover, Fig. 21 shows the contour plots of von Mises stress obtained by two numerical methods. As shown in the results, the max von Mises stresses obtained by our method with four sets of source points are almost the same. Moreover, the result obtained by 738 source points is within 0.3% of the reference solution. It is to say that our method with a few source nodes can achieve an acceptable engineering accuracy. Thus, this numerical example illustrates the ability of our method to solve the practical problems in engineering.

6. Conclusions

Considering the physical relationship between the displacements and tractions, we firstly present a novel Hermite-type approximation for elasticity problems in this paper. Then, employing Hermite-type approximation instead of MLS approximation as the second-layer interpolation in the DiBFM, we propose a novel DiBFM with Hermite-type approximation for elasticity problems. Compared with the standard MLS approximation, the Hermite-type approximation has two advantages. First, the shape functions in Hermite-type approximation are constructed with Cartesian coordinates, while parameter coordinates are employed in MLS approximation. Second, the influence domain in Hermite-type approximation can cover multiple edges, whereas it is restricted in only one edge in MLS approximation.

The proposed method can attain high accuracy and efficiency, the same as the original DiBFM. Meanwhile, based on the second feature of Hermite-type approximation, the novel method is superior to the original DiBFM in handling structures with thin walls and small features, even the length ratio reaching to 10^3. Numerical examples with engineering background have illustrated the accuracy, efficiency and practicality of the proposed method. In future work, we are going to develop the method to solve crack propagation problem and extend to solve 3D case.

Declaration of competing interest

On behalf of all authors, the corresponding author states that there is no conflict of interest.

CRediT authorship contribution statement

Jianming Zhang: Conceptualization, Methodology, Software, Writing - original draft. **Rui He:** Software, Methodology, Investigation, Writing - review & editing. **Weicheng Lin:** Supervision, Methodology, Writing - review & editing. **Le Yang:** Methodology, Writing - review & editing. **Baotao Chi:** Visualization, Writing - review & editing. **Chuanming Ju:** Validation, Writing - review & editing. **Suliman:** Writing - review & editing.

Acknowledgements

This work was supported by National Natural Science Foundation of China under grant numbers 11772125 and 11972010.

References

Belytschko, T., Krongauz, Y., Organ, D., Fleming, M., Krysl, P., 1996. Meshless methods: an overview and recent developments. Comput. Methods Appl. Mech. Eng. 139 (1–4), 3–47.

Cheng, A.D., Chen, C.S., Golberg, M.A., Rashed, Y.F., 2001. BEM for thermoelasticity and elasticity with body force-a revisit. Eng. Anal. Bound. Elem. 25 (4–5), 377–387.

Cisilino, A.P., Aliabadi, M.H., 2004. Dual boundary element assessment of three-dimensional fatigue crack growth. Eng. Anal. Bound. Elem. 28 (9), 1157–1173.

Cruse, T.A., 2012. Boundary Element Analysis in Computational Fracture Mechanics, vol. 1. Springer Science & Business Media.

Deng, Q., Li, C.G., Wang, S.L., Tang, H., Zheng, H., 2013. A new method to the treatment of corners in the BEM, Engineering Analysis with Boundary Elements, 37 (1), 182–186.

Dong, C.Y., Lo, S.H., Cheung, Y.K., 2002. Application of the boundary-domain integral equation in elastic inclusion problems. Eng. Anal. Bound. Elem. 26 (6), 471–477.

Duarte, C.A., Oden, J.T., 1996. H-p clouds-An h-p meshless method, Numerical Methods for Partial Differential Equations. Int. J. 12 (6), 673–705.

Florez, W.F., Power, H., 2001. Comparison between continuous and discontinuous boundary elements in the multidomain dual reciprocity method for the solution of the two-dimensional Navier–Stokes equations. Eng. Anal. Bound. Elem. 25 (1), 57–69.

Garrido, J.A., Foces, A., Paris, F., 1991. BEM applied to receding contact problems with friction. Math. Comput. Model. 15 (3–5), 143–153.

Johnston, B.M., Johnston, P.R., Elliott, D., 2013. A new method for the numerical evaluation of nearly singular integrals on triangular elements in the 3D boundary element method. J. Comput. Appl. Math. 245, 148–161.

Lancaster, P., Salkauskas, K., 1981. Surfaces generated by moving least squares methods. Math. Comput. 37 (155), 141–158.

Li, G., Aluru, N.R., 2002. Boundary cloud method: a combined scattered point/boundary integral approach for boundary-only analysis. Comput. Methods Appl. Mech. Eng. 191 (21–22), 2337–2370.

Li, G., Aluru, N.R., 2003. A boundary cloud method with a cloud-by-cloud polynomial basis. Eng. Anal. Bound. Elem. 27 (1), 57–71.

Li, X.L., Zhu, J.L., 2009. A meshless Galerkin method for Stokes problems using boundary integral equations. Comput. Methods Appl. Mech. Eng. 198 (37–40), 2874–2885.

Li, Y., Zhang, J.M., Yu, L.X., Lu, C.J., Li, G.Y., 2015. GPU-accelerated regular integration and singular integration in boundary face method. Aust. J. Mech. Eng. 13 (3), 163–171.

Liu, Y.J., Nishimura, N., 2006. The fast multipole boundary element method for potential problems: a tutorial. Eng. Anal. Bound. Elem. 30 (5), 371–381.

Manolis, G.D., Banerjee, P.K., 1986. Conforming versus non-conforming boundary elements in three-dimensional elastostatic. Int. J. Numer. Methods Eng. 23 (10), 1885–1904.

Mitra, A.K., Ingber, M.S., 1993. A multiple-node method to resolve the difficulties in the boundary integral equation method caused by corners and discontinuous boundary conditions. Int. J. Numer. Methods Eng. 36 (10), 1735–1746.

Parreira, P., 1988. On the accuracy of continuous and discontinuous boundary elements. Eng. Anal. 5 (4), 205–211.

Ribeiro, T.S.A., Beer, G., Dünser, C., 2008. Efficient elastoplastic analysis with the boundary element method. Comput. Mech. 41 (5), 715–732.

Shrivastava, V., Aluru, N.R., 2003. A fast boundary cloud method for exterior 2D electrostatic analysis. Int. J. Numer. Methods Eng. 56 (2), 239–260.

Shu, X.M., Zhang, J.M., Han, L., Dong, Y.Q., 2016. A surface-to-surface scheme for 3D contact problems by boundary face method. Eng. Anal. Bound. Elem. 70, 23–30.

Telles, J.C.F., Brebbia, C.A., 1981. Boundary element solution for half-plane problems. Int. J. Solid Struct. 17 (12), 1149–1158.

Wang, X.H., Zhang, J.M., Zhou, F.L., Zheng, X.S., 2013. An adaptive fast multipole boundary face method with higher order elements for acoustic problems in three-dimension. Eng. Anal. Bound. Elem. 37 (1), 144–152.

Wen, P.H., Aliabadi, M.H., Rooke, D.P., 1998. Cracks in three dimensions: a dynamic dual boundary element analysis. Comput. Methods Appl. Mech. Eng. 167 (1–2), 139–151.

Yao, Z.H., Kong, F.Z., Wang, H.T., Wang, P.B., 2004. 2D simulation of composite materials using BEM. Eng. Anal. Bound. Elem. 28 (8), 927–935.

Ye, W.J., 2008. A new transformation technique for evaluating nearly singular integrals. Comput. Mech. 42 (3), 457.

Zhang, J.M., Qin, X.Y., Han, X., 2009. A boundary face method for potential problems in three dimensions. Int. J. Numer. Methods Eng. 80, 320–337.

Zhang, Y.M., Gu, Y., Chen, J.T., 2011. Stress analysis for multilayered coating systems using semi-analytical BEM with geometric non-linearities. Comput. Mech. 47 (5), 493–504.

Zhang, J.M., Han, L., Lin, W.C., Dong, Y.Q., Ju, C.M., 2017a. A new implementation of BEM by an expanding element interpolation method. Eng. Anal. Bound. Elem. 78, 1–7.

Zhang, J.M., Lin, W.C., Dong, Y.Q., 2017b. A double-layer interpolation method for implementation of BEM analysis of problems in potential theory. Appl. Math. Model. 51, 250–269.

Zhang, J.M., Lin, W.C., Dong, Y.Q., 2019a. A dual interpolation boundary face method for elasticity problems. Eur. J. Mech. Solid. 73, 500–511.

Zhang, J.M., Dong, Y.Q., Lin, W.C., Ju, C.M., 2019b. A singular element based on dual interpolation BFM for V-shaped notches. Appl. Math. Model. 71, 208–222.

Zhang, J.M., Shu, X.M., Trevelyan, J., Lin, W.C., Chai, P.F., 2019c. A solution approach for contact problems based on the dual interpolation boundary face method. Appl. Math. Model. 70, 643–658.

Zhou, F.L., Zhang, J.M., Sheng, X.M., Li, G.Y., 2012. A dual reciprocity boundary face method for 3D non-homogeneous elasticity problems. Eng. Anal. Bound. Elem. 36 (9), 1301–1310.